sustainability

MDPI

Article

Numerical Evaluation of Suction Effects and Groundwater Table Variations on Long-Term Pavement Subgrade Performance

Siva Ram Karumanchi [1], Anirban Mandal [2,*] and Stanislav Lenart [1,*]

[1] Slovenian National Building and Civil Engineering Institute (ZAG), 1000 Ljubljana, Slovenia; ram.karumanchi@zag.si
[2] Visvesvaraya National Institute of Technology, Nagpur 440010, India
* Correspondence: amandalthesis@yahoo.com (A.M.); stanislav.lenart@zag.si (S.L.); Tel.: +91-9158199911 (A.M.); +386-31347826 (S.L.)

Abstract: Over the past few decades, flexible pavements across the globe have seen a significant reduction in their service life due to climate changes. The flexible pavements with unsaturated subgrades undergo volumetric changes during the drying and wetting phases, affecting their long-term deformation behavior. These phases cause significant variations in matric suction and groundwater table depth. This study employs a coupled pore pressure-deformation analysis on flexible pavements to investigate the impact of groundwater table depth and suction variations in unsaturated subgrades. Finite-element simulations using the Abaqus and developed USDFLD code were validated against literature data. Sensitivity analysis was conducted by varying the suctions in subgrades during drying and subsequent wetting to evaluate the groundwater table depth. Furthermore, under heavy cyclic wheel loading, pavement-deformation analysis was conducted to investigate the influence of subgrade suction. The findings demonstrate that, after an initial drying phase at 5000 kPa suction, wetting over 180 days caused the groundwater level to rise from 5.45 m beneath the subgrade to the surface. This led to a 98% increase in surface-vertical deformations due to cyclic wheel loading after 180 days of wetting compared to the deformations during the drying phase at the same suction level. This assessment of groundwater-depth variations and long-term deformation behavior with the impact of suction improves the design and sustainability of flexible pavements.

Keywords: flexible pavement; unsaturated soil; suction; finite-element method

Citation: Karumanchi, S.R.; Mandal, A.; Lenart, S. Numerical Evaluation of Suction Effects and Groundwater Table Variations on Long-Term Pavement Subgrade Performance. *Sustainability* **2024**, *16*, 9469. https://doi.org/10.3390/su16219469

Academic Editors: José Neves, Ana Cristina Freire and Vítor Antunes

Received: 20 September 2024
Revised: 9 October 2024
Accepted: 22 October 2024
Published: 31 October 2024

1. Introduction

Climatic changes can cause permanent deformations in flexible pavements with unsaturated subgrades, particularly in arid and semi-arid regions. The subgrade moisture eventually reaches equilibrium after construction under stable environmental conditions. However, this equilibrium can be disturbed due to rainfall infiltration and subsequent drying of the subgrade. The sustainability of flexible pavements in the long run is impacted by various climatic factors such as surface and ground temperature, rainfall, humidity, and groundwater levels [1]. According to the Indian Meteorological Department (IMD), the surface temperatures measured in most parts of the country from years 1980 to 2020 range between 28–45 °C in the pre-monsoon period, 24–35 °C during the monsoon, and 15–28 °C in the post-monsoon period [2]. Moreover, heavy rainfall frequently occurs during monsoons and cyclones across different parts of India, with daily downpours ranging between 10 mm and 500 mm [3]. Studies indicated that these climatic changes severely damage various railway and road infrastructures [1,3–6]. Moisture fluctuations resulting from climatic changes lead to rapid variations in groundwater table depth. These variations create different saturation stages in subgrade soil in semi-arid climates. At various saturation levels, capillary forces resulting in suction may form in the subgrade soil, which increases the inter-particle forces. As a result, the subgrade soil can experience

volume changes during drying and subsequent wetting, which may affect the long-term performance and sustainability of flexible pavements, potentially leading to significant deformations at the pavement surface. In addition, the rapid rainfall infiltration causes extensive damage to flexible pavements. The damages to flexible pavement include surface roughness, rutting, upheaval, and the development of longitudinal and fatigue cracks [7,8]. Researchers [9] reported distress in pavements even before traffic loading in the form of dry land cracks due to increased shrinkage stresses. In addition, moisture changes in the subgrade influence the pavement-deformation characteristics [10]. Considering these factors, researchers analyzed crack patterns in pavements, the performance of moisture barriers [11,12], pavement-stability problems in transient conditions [13,14], and the influence of vegetation on the unsaturated ground [15,16]. These studies indicate that suction is an essential parameter in evaluating the long-term performance of pavements. Hence, they recommended using a soil-water characteristic curve relating to moisture and suction to analyze unsaturated soil.

The suction variations in unsaturated soil induce significant changes in its stiffness [17–19]. This shows that the mechanical behavior of the unsaturated subgrade is controlled by the moisture and suction changes [20]. The suction variations considerably affect the associated stresses and strains [21]. However, the stresses and strains associated with suction are often not considered for analyzing unsaturated soil subgrades. Further, researchers assumed recoverable deformations of pavements under the repeated application of moving traffic loads. Accordingly, they proposed design recommendations considering the linear–elastic behavior of the surface layer, base, and elastoplastic behavior subgrade. However, coupled suction and elastoplastic behavior of subgrade may result in permanent ground deformations [22,23]. Hence, this coupled behavior is needed to quantify the realistic deformations in pavements. This type of analysis is instrumental in deciding the design requirements of sustainable pavements, such as the thickness of the base and sub-base course, side drainage, and appropriate maintenance of the depth of the groundwater table (d_{gwt}). In this context, there is a need to evaluate the unsaturated subgrades by developing a framework integrating suction in its elastoplastic constitutive behavior. Therefore, to address this research need, a coupled pore pressure-deformation analysis was conducted on flexible pavements with unsaturated subgrade to study the changes in d_{gwt} with respect to suction variations during drying and wetting. The developed coupled numerical model was used to conduct sensitive analysis by varying the suctions to assess the pavement deformations under heavy cyclic wheel loading.

2. Incorporation of Associated Stresses and Strains with Suction Changes

Unlike a saturated system, the choice of stress space for partially saturated soil is more complicated. Numerous efforts are made to describe the mechanical behavior of unsaturated soil with a single effective stress [24]. Bishop (1959) suggested the effective stress concept (Equation (1)) for partially saturated soil consistent with traditionally used saturated soil mechanics proposed by Terzaghi (1943) [24–27].

$$\sigma'_{ij} = \sigma_{ij} - u_a\delta_{ij} + \chi(u_a - u_w)\delta_{ij} \quad (1)$$

where σ'_{ij} is the effective stress, σ_{ij} is the total stress, $u_a - u_w$ is the matric suction, δ_{ij} is Kronecker's delta, and χ is the effective stress parameter varying from 0 to 1. However, limitations in describing stress states with single effective stress-state parameters lead to difficulty modeling the deformation behavior of partially saturated soils [24,26,27]. The volumetric changes in unsaturated soil are associated with net normal stress and matric suction. Fredlund (1979) [28] proposed two stress-state variables for constitutive relationships: net normal stress and matric suction. In addition to the matric suction, there might be a small contribution of osmotic suction to volumetric changes. Incorporating

these parameters, a simplified model to predict volumetric strains produced in unsaturated soil is provided in Equation (2) [9]

$$\frac{\nabla V}{V} = -\gamma_s \log\left(\frac{s_f}{s_i}\right) - \gamma_\sigma \log\left(\frac{\sigma_f}{\sigma_i}\right) - \gamma_\varphi \log\left(\frac{\varphi_f}{\varphi_i}\right) \quad (2)$$

where, γ_s, γ_σ, γ_φ are the compression indices corresponding to matric suction, mean principle stress, and osmotic suction, respectively, s_f, σ_f, φ_f are the respective final matric suction, mean principle stress, and osmotic suction, s_i, σ_i, φ_i are initial matric suction, mean principle stress, and osmotic suction, and ∇V is the change in the volume of the elemental soil. These compression indices are obtained from laboratory measurements or can be estimated from developed empirical relationships. The impact of osmotic suction is rarely observed without sulfates in unsaturated soil subgrade. Further, the subgrade during construction does not experience traffic loading. Therefore, for no external loading and no osmotic suction, the volumetric changes are produced only by the matric suction component, as shown in Equation (3) [9,28,29]:

$$\frac{\nabla V}{V} = -\gamma_s \log\left(\frac{s_f}{s_i}\right) \quad (3)$$

For expansive soil with a lateral constraint, higher vertical strains lead to roughness development in pavements [29]. The unsaturated soil will have strain components with corresponding displacements and matric suction. The suction-induced strain components are obtained from Equation (4) [9].

$$\varepsilon_{xx} = \varepsilon_{yy} = \varepsilon_{zz} = -\frac{1}{3}\gamma_s \log\left(\frac{s_f}{s_i}\right) \quad (4)$$

The superimposition of suction-induced strains with stresses due to self-weight provides [9]:

$$\varepsilon_{xx} = \frac{1}{E}\left(\sigma_{xx} - v\sigma_{yy} - v\sigma_{zz}\right) + \left[-\frac{1}{3}\gamma_s log\left(\frac{s_f}{s_i}\right)\right] \quad (5)$$

$$\varepsilon_{yy} = \frac{1}{E}\left(\sigma_{yy} - v\sigma_{xx} - v\sigma_{zz}\right) + \left[-\frac{1}{3}\gamma_s log\left(\frac{s_f}{s_i}\right)\right] \quad (6)$$

$$\varepsilon_{zz} = \frac{1}{E}\left(\sigma_{zz} - v\sigma_{xx} - v\sigma_{yy}\right) + \left[-\frac{1}{3}\gamma_s log\left(\frac{s_f}{s_i}\right)\right] \quad (7)$$

3. Implementation of Suction-Dependent Shear Strength and Modulus of Elasticity for Finite-Element Model Simulations

Several powerful numerical techniques, such as the Finite-Difference Method (FDM) [30], Discrete-Element Method (DEM) [31], Finite-Element Method (FEM) [7,32,33], and Bezier Multi-Step Method [34], have been developed to handle complex coupled pore pressure and deformation analyses of flexible pavements with unsaturated subgrades. The present investigation used finite-element simulations for coupled pore pressure-deformation analysis, with a modified material model implemented through a user-defined subroutine for field variables (USDFLD). The structural performance of pavements is primarily dependent on the shear strength behavior of subgrade soils. Hence, in general practice, pavement subgrades are designed based on the conventional shear-strength theory. However, in most scenarios, the subgrade will be in an unsaturated condition, indicating the influence of suction characteristics on the shear-strength behavior of the subgrade material. Fredlund et. al, 2012 [35] proposed a rational framework for interpreting the mechanical behavior of unsaturated soils in terms of two independent stress-state variables: net normal stress and matric suction (u_a–u_w). They proposed a shear-strength relationship extending the Mohr–Coulomb failure criterion for unsaturated soils in terms of two stress-state variables. Many experimental studies have been conducted over the last few decades to determine

and interpret the shear strength of unsaturated soils (SSUS) following this framework. The equation proposed by Fredlund et al., 2012 [35] was a valuable tool for explaining the shear-strength change from a saturated condition to an unsaturated condition, and vice versa.

It is found that the angle of friction (φ′) of soil is not affected by the matric suction; the total cohesion for unsaturated soil can be defined by taking the first and third terms of Equation (3) together [23]. Researchers [19] reported that the suction highly influences the modulus of elasticity of the unsaturated soil. Oh et al., 2009 [17] proposed the equation of cohesion and modulus of elasticity for unsaturated soil to predict the response due to suction variation using the soil water characteristic curve (SWCC) and cohesion and modulus of elasticity of saturated soil.

Variation of cohesion with respect to matric suction in unsaturated soil [17]:

$$c'_{unsat} = c'_{sat}\left[1 + \frac{(u_a - u_w)}{(P_a/100)}\left(s^V\right)/\mu\right] \tag{8}$$

Variation of elastic modulus with respect to matric suction in unsaturated soil [17]:

$$E_{unsat} = E_{sat}\left[1 + \alpha\frac{(u_a - u_w)}{(P_a/100)}\left(s^\beta\right)\right] \tag{9}$$

where c' and E_a are the cohesion and modulus of elasticity for saturated soil, s is the degree of saturation, P_a is the atmospheric pressure in kPa, and β, α, V, μ are the fitting parameters. Equations (8) and (9) are included in the Mohr–Coulomb material model to capture the variation of the response of unsaturated soil with suction. To incorporate this, the user subroutine USDFLD code is written, implemented, and integrated for model updating in the Abaqus.

4. Model Description

This study investigates the performance of flexible pavements with unsaturated subgrade made of fine-grained soil. For this purpose, a coupled pore pressure-deformation analysis is considered to analyze the flexible pavements with subgrade in saturated and unsaturated conditions. The changes in the depth groundwater table (d_{gwt}) with respect to suction variations during drying and wetting were investigated. In addition, the impact of cyclic wheel loads on the pavement surface deformations during drying and wetting was estimated. The following assumptions were considered for modeling and simulations: (1) A three-layer model was considered with base, sub-base, and subgrade. (2) The analysis was considered in undrained conditions. (3) Cyclic wheel loading was considered. (4) Side drainage was not considered in the analysis. In this study, an undrained condition was assumed for saturated soil subgrades to replicate real-world conditions where low permeability restricts drainage, causing pore pressure buildup under repeated loading. For unsaturated soils, suction-dependent behavior was incorporated to reflect moisture fluctuations and their influence on the mechanical characteristics of the subgrade. This allows us to capture the changing stiffness and strength in unsaturated soils under different suction levels and the impact of drying and wetting cycles on the subgrade. Although side drainage is vital for controlling moisture gain and loss in real-world pavements, the primary objective of this study was to investigate the direct relationship between suction, groundwater depth, and vertical pavement deformation. By isolating these factors, this study aims to develop a clearer understanding of the fundamental behavior of flexible pavements with unsaturated subgrade under cyclic loading.

The present study mainly focuses on different subgrade parameters affecting pavement performance and, in particular, evaluating the effect of suction on the changes in the groundwater table (g_{wt}) and its impact on the pavement structural deterioration. An axis-symmetric two-dimensional (2D) finite-element model of a flexible pavement with an unsaturated subgrade overlaid with a granular base and asphalt concrete (AC) layer

was developed. Figure 1 shows the geometrical illustration of the three-layer system of the pavement model considered in the present study. The boundary effects were tackled by adopting optimized dimensions of the model. Hence, the adopted depth and width of the subgrade were 5 m and 10 m, respectively, and the thickness of the base and AC layer were considered as 0.4 m and 0.1 m, respectively. For three-dimensional (3D) analysis, a significant computation time is required for the coupled deformation pore-pressure analysis. There are high chances of overestimating the pavement response from a typical 2D plane-strain model. Further, researchers [10,36,37] found that 2D axis-symmetric analysis showed no substantial loss of accuracy when compared to 3D analysis, with similar pavement deformation behavior being observed. In addition, a 2D axis-symmetric model considers cylindrical coordinate systems with constant properties in all horizontal planes. Therefore, the 2D axis-symmetric model was considered for coupled deformation pore-pressure analysis to reduce the computation time and obtain an appropriate pavement response. The considered boundary conditions for the model were that the base was restrained from moving in horizontal and vertical directions. The vertical boundaries were restrained from moving in the horizontal direction. Water flow is not allowed at the base and sides of the model. The simulation of the numerical model was done using the Abaqus finite-element code. The AC and base layer are discretized with a four-node quadrilateral axis-symmetric element considering bilinear displacement. The subgrade is discretized with a four-node axis-symmetric quadrilateral, bilinear displacement, and bilinear pore pressure for simulating coupled pore-pressure deformation analysis. An element size of 0.1 × 0.04 m was applied for the region covering the wheel load. A typical element size of 0.1 × 0.1 m was considered for the remaining model, as shown in Figure 2.

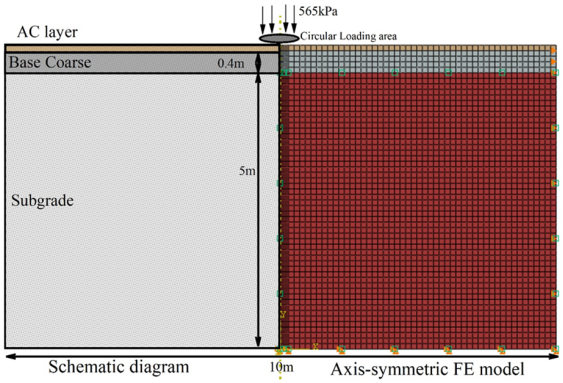

Figure 1. Illustration of the pavement section.

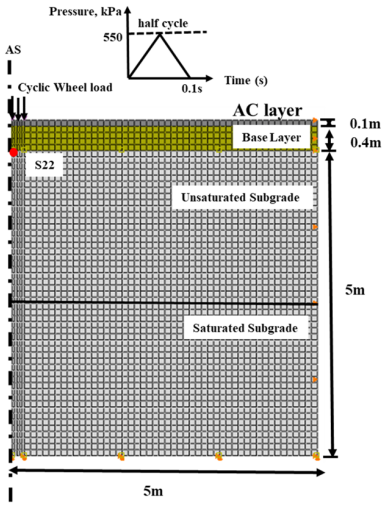

Figure 2. Illustration of axis-symmetric FE model.

5. Material Behavior

An elastoplastic framework is needed to solve boundary-value problems in geotechnical engineering practice. The present study considered a modified elastoplastic model for the subgrade and a Drucker–Prager model for the base layer with parameters given in Table 1. Further, it was found that the stiffness and shear strength of unsaturated soil depends on the matric suction [19]. This dependency should be included in the material model to capture the response of unsaturated soil. In this study, the dependence of stiffness and strength on suction, as provided in Table 2, was adopted from the empirical relations presented in Equations (8) and (9). As discussed, the changes in matric suction (negative *pwp*) were incorporated into the analysis as a field variable, influencing the elastic modulus and cohesion. The fitting parameters $\beta = 2$, $\alpha = 0.05$, $V = 2$, and $\mu = 62.5$ were adopted for the subgrade with fine-grained soil and a plasticity index greater than 30 [17,38]. These empirical equations are included in the Mohr–Coulomb material model through user subroutine USDFLD provided in Appendix A to predict the response of unsaturated soil. Hence, a modified Mohr–Coulomb material model is used to capture the behavior of subgrade material, and the corresponding material parameters are provided in Table 1.

Table 1. Parameters for base material and subgrade soil considered for adopted pavement model.

Parameters	Base	Subgrade
% Fines (Passing Sieve No 200)	0	80
Specific Gravity	2.60	2.53
Initial Void Ratio	0.25	0.590
Initial Saturation	-	0.88
Saturated modulus of elasticity, E (kPa)	100,000	3000
Poisson's Ratio	0.3	0.3
Saturated cohesion, E (kPa)	0	10
Angle of Friction (°)	50	10
Permeability (m/s)	0.008	6.1×10^{-10}
Density (kN/m^3)	22	15.4

Table 2. Elastic modulus and cohesion variation with matric suction.

Matric Suction kPa	Degree of Saturation	E_{unsat} kPa	C_{unsat} kPa
−5000	0.4	123,000	138
−2500	0.5	96,750	110
−1250	0.7	94,875	108
−1000	0.75	87,375	100
−750	0.8	75,000	86.8
−500	0.85	57,187.5	67.8
−100	0.95	16,537.5	24.44
0	1	3000	10

The elastic modulus of the base granular material was assumed to be 100,000 kPa, as provided in Table 1. The AC layer parameters considered for the simulations are adopted from published research to represent realistic material characteristics, as evaluated in the scope of the reduced model test performed by Gu et al. (2016) [37]. In addition, change in moisture with respect to suction was considered for the subgrade soil by incorporating the suction-saturation variations, as shown in Table 2 [39]. The AC layer is generally treated

as an elastic material. However, due to its viscoelastic nature, it dissipates energy, leading to permanent deformations of the pavement surface. Hence, to capture the viscoelastic behavior of the AC layer, parameters from the dynamic modulus test were adopted, as shown in Table 3 [37]. The relaxation shear and bulk modulus were interconverted from the Prony series model to simulate the time-dependent viscoelastic behavior of the AC layer.

Table 3. Parameters for AC layer adopted from Gu et al., 2016 [37].

	Coefficients of Prony Series		
	$\mathbf{G_i}$	$\mathbf{K_i}$	τ_i
1	0.362	0.362	4.09×10^{-6}
2	0.363	0.363	2.56×10^{-4}
3	0.1765	0.1765	7.71×10^{-3}
4	0.074	0.074	2.10×10^{-1}
5	0.0165	0.0165	3.88×10^{0}
6	0.0057	0.0057	6.53×10

6. Loading History and Pavement Contact Area

The traffic load is one of the critical parameters in determining the long-term performance of pavements. The loading parameters affecting the pavement performance are the type of wheel load, the contact area of wheels, load reputations, and vehicle speed. The base of the wheel was assumed to be rigid. In general, the rectangular contact area is not axis-symmetric. Thus, the pavement surface in the present study was subjected to cyclic wheel loading distributed to an equivalent circular contact area (Figures 1 and 2). A heavy traffic cyclic wheel loading at the pavement's center was adopted for the analysis [40]. The wheel loading was assumed as an impulse type with a load amplitude equal to half of a heavy vehicle's axle load (single wheel axle load = 40 kN). The wheel load was applied on the surface of the pavement with a circular contact area of 0.07065 m^2 (P = 565 kPa). In addition, the impulse type of loading was used considering an average vehicle speed of 80 kph repeated for 10,000 cycles to accommodate cyclic loading.

7. Model Validation

In finite-element analysis, the stress-deformation mechanism resulting from external loads in unsaturated soil, considering suction, differs from the mechanism observed in conventionally saturated soil. This study included validations to replicate the behavior of unsaturated soil and evaluate pavement-surface deformations. In this context, results of two previous studies have been used to validate the efficacy of the developed numerical model: (1) An FE model to explore the effects of external static loads on unsaturated soil with varying groundwater table depths, adopted from Cheng et al., 2021 [18], and (2) an FE model assessing the impact of external loads on pavement, utilizing the data and results from Gu et al., 2016 [37].

7.1. Model Validation of Suction-Induced Deformations

A two-dimensional finite-element model of soil with 14 m × 12 m (height × width) has been modelled in Abaqus as shown in Figure 3a. A strip footing with a width of 2 m is placed on top of the soil. The foundation soil is discretized with a four-node plane strain quadrilateral, bilinear displacement, bilinear pore pressure, and reduced integration mesh (CPE4RP) for simulating coupled pore-pressure deformation analysis. An element size of 0.5 × 0.2 m was applied for the region covering the footing load, whereas, for the remaining model, a common element size of 0.5 × 0.4 m is considered. The boundary conditions for the model were applied in such a way that the base was restrained to move in horizontal and vertical directions. The vertical boundaries were restrained to

move in the horizontal direction. Water flow is not allowed at the base and sides of the model. The Mohr–Coulomb material model is used to simulate the response of the soil. The material parameters considered for the simulations are adopted from Cheng et al., 2021 [18], as shown in Table 4. The fitting parameters β, α, V, and μ are considered as 2, 20, 2, and 0.1 based on the behavior of fine-grained unsaturated soil and the width of strip footing [18,23,41,42]. In addition, change in moisture with respect to suction was considered for the foundation soil by incorporating the soil–water characteristic curve (SWCC). The SWCC (as shown in Figure 3b) considered in this study is adopted from [18]. Figure 3c depicts the vertical stress versus displacement response of foundation soil for four different groundwater table depths without using the USDFLD user subroutine code in Abaqus. In this obtained result, we can observe that the elastoplastic Mohr–Coulomb-type behavior of soil cannot capture the variation of response of soil due to changes in the depth of the groundwater table. However, the effect of variation of matric suction on soil response can be observed in Figure 3d. As the depth of groundwater goes deeper, the matric suction in soil increases and contributes to a higher cohesion and modulus of elasticity. The higher value of cohesion and modulus of elasticity provides a higher stress value at failure with a lower level of displacement. A similar type of behavior has also been observed by Cheng et al., 2021 [18] in their numerical analysis performed on a shallow foundation resting on unsaturated soil. This confirms the applicability of the developed numerical framework, a USDFLD code that incorporates suction characteristics into the Mohr–Coulomb-type elastoplastic constitutive model.

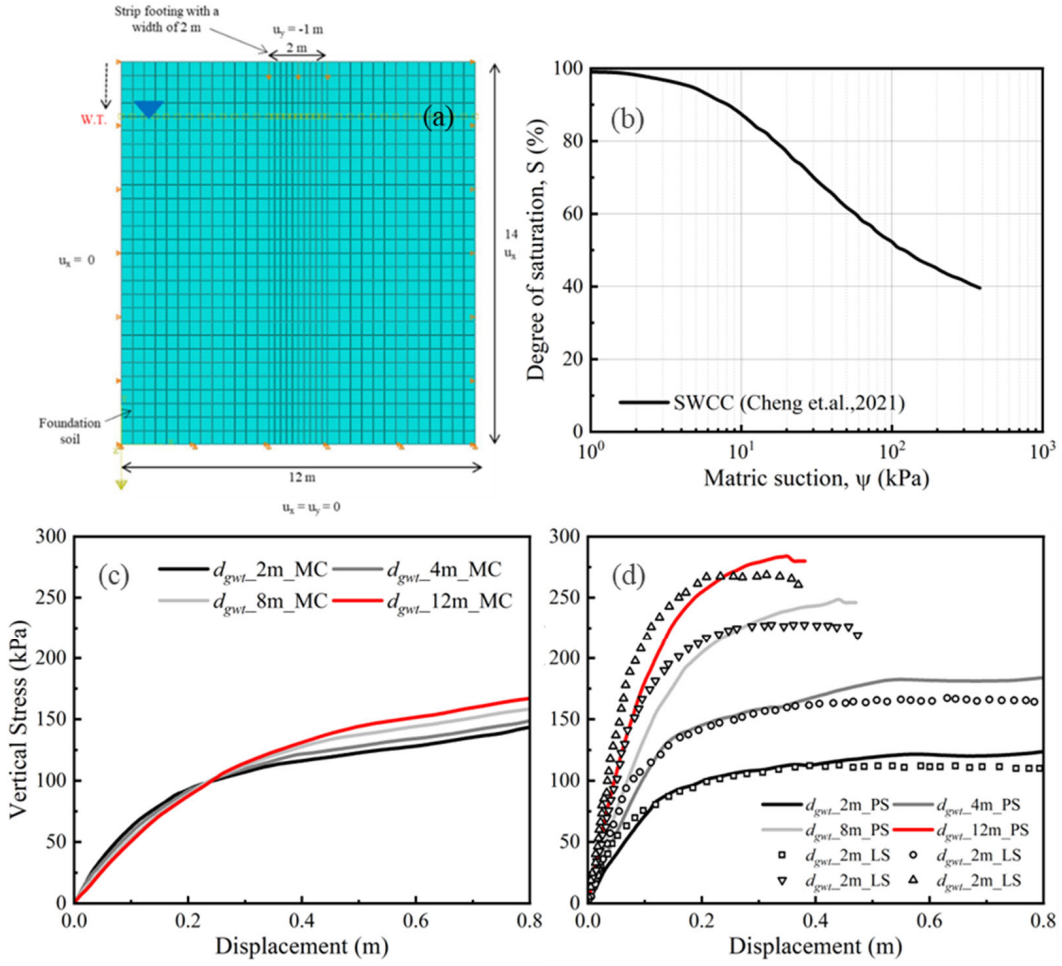

Figure 3. (**a**) Illustration of 2D FE-strip footing model with varying g_{wt} below the ground surface; (**b**) soil water characteristic curve adopted from Cheng et al., 2021 [18]; (**c**) vertical stress versus displacement response without USDFLD; (**d**) vertical stress versus displacement response with USDFLD.

Table 4. Parameters for soil considered for pavement model adopted from Cheng et al., 2021 [18].

Parameters	Value
Dry density, γd (kN/m^3)	13.92
Saturated cohesion, c′ (kPa)	13.1
Saturated modulus of elasticity, E (kPa)	3516
Poisson's ratio, ν	0.37
Saturated undrained shear strength, $\frac{q_u}{2}$ (kPa)	13.1
Specific gravity	2.72

7.2. Model Validation of Cyclic Load-Induced Deformations

The FE pavement model was validated from the reduced model test data obtained from Gu et al., 2016 [37]. The vertical deflection behavior of the pavement was analyzed for validation. The FE model was similar to a pavement-testing program (Figure 4a) from a large-scale circular test tank developed by Gu et al., 2016 [37]. The outer dimensions of the circular tank are 2.4 m in diameter and 1.8 m in height, including a 0.15 m AC layer, 0.15 m base course layer, and 1.50 m subgrade. The pavement structure was subjected to a 565 kPa load on a circular area of 0.15 m radius. The summary of material parameters is provided in Tables 3 and 5. Further, Li et al., 2019 [43] numerically analyzed a similar pavement structure considering a user-defined constitutive model to accommodate the moisture-dependent behavior of unsaturated subgrade.

The results of this approach are also presented. Figure 4b shows that as the distance to the center of the load increases, the measured and predicted road-surface deflection gradually decreases. Meanwhile, the results of both models are similar to the actual measured response of pavement structure. The main cause of measurement error is that the strength of pavement materials is enhanced by the steel tank's cyclic hoop effect. The slight difference in results and present analysis is due to different constitutive models; Li et al., 2019 [43] used a user-defined constitutive model, whereas in the present study, the Mohr–Coulomb material model was used for the analysis. In addition, the good agreements indicate the applicability and correctness of the developed pavement model.

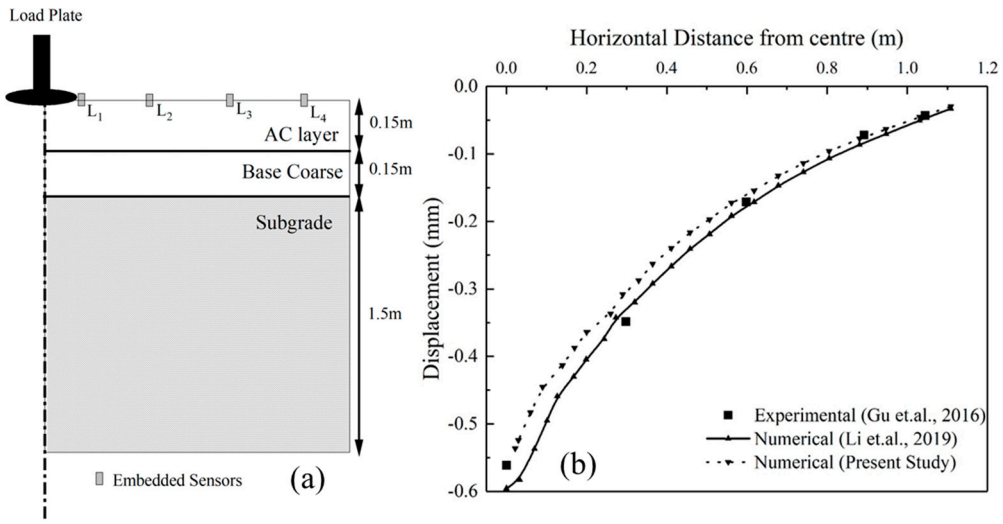

Figure 4. (**a**) Illustration of the experimental model adopted from Gu et al., 2016 [37], Li et al., 2019 [43] for validation; (**b**) results of numerical validation.

Table 5. Parameters for base material and subgrade soil considered for validation model adopted from Gu et al., 2016 [37].

Parameters	Base	Subgrade
Specific Gravity	2.60	2.53
Initial Void Ratio	0.25	0.590
Initial Saturation	-	0.88
Modulus of elasticity, E (kPa)	56,000	40,000
Poisson's Ratio	0.3	0.3
Cohesion (kPa)	0	40
Angle of Friction (°)	50	10
Permeability (m/s)	0.008	6.1×10^{-10}

8. Simulation Results and Discussion

The distribution of suction in the subgrade was obtained using initial and final suctions as boundary conditions. The *pwp* of zero represents the g_{wt} surface, and the negative *pwp* at the subgrade top was provided depending on the assumed suction state. The influence of suction on the subgrade during drying was studied by analyzing the four enforced suction states at the top of the subgrade soil; Ψ_t = 500 kPa, Ψ_t = 1250 kPa, Ψ_t = 2500 kPa, and Ψ_t = 5000 kPa, respectively, for a duration of 0–180 days. Further, the pavement response for the wheel loading is examined with subgrade in unsaturated and saturated conditions.

8.1. The Effect of Subgrade Drying

For the analysis purpose, three sequential steps were considered during drying: (1) A geostatic step simulating the in situ conditions of the subgrade soil before the construction of the base and AC layers; (2) a soil step to simulate the suction behavior in subgrade soil (in this step, base and AC layers are also included); (3) application of the wheel load. The SWCC data as shown in Table 2 were used to estimate the suction profile in the unsaturated subgrade.

8.1.1. In Situ Conditions and Changes in g_{wt} with Subgrade Suction During Drying

Initially, the subgrade soil was analyzed for geostatic conditions in which it was assumed that the g_{wt} is at the top. The subgrade soil under consideration exhibits low permeability and lower stiffness. The effective stresses and pore water pressure (*pwp*) at 5 m below the subgrade appeared to be 49 kPa and 26.5 kPa, respectively. In the geostatic analysis condition, the deformations produced in the soil system are negligible. In the subsequent step, drying of the subgrade was initiated, which was continued for a 1-to-180-day time period. The analysis considered four cases where subgrade suctions at the top were enforced at levels of Ψ_t = 1250 kPa, Ψ_t = 500 kPa, Ψ_t = 5000 kPa, and Ψ_t = 2500 kPa, respectively, for a duration of 1, 10, 30, 60, 90, 120, and 180 days. During the drying process, the g_{wt} decreases, and suction (negative *pwp*) in the unsaturated soil changes along the depth of the subgrade. Further, different time durations for the drying process have been chosen to evaluate the changes in g_{wt} from the *pwp* distributions along the depth of the subgrade. The contour of the *pwp* distribution in the subgrade at in situ geostatic condition with g_{wt} at the top is depicted in Figure 5a. This figure indicates a linear variation of *pwp*, or 0–50 kPa (consistent with the theoretical value at 5 m of depth, $\gamma_w h = 5 * 9.81 = 49$ kPa), along the subgrade depth. Subsequently, Figure 5b–h indicates the contour depictions of the case Ψ-1250, where a suction of 1250 kPa is enforced at the top for 180 days. In these figures, the contours are depicted in terms of *pwp* which can be positive or negative, while the negative *pwp* represents suction. Further, the red horizontal line marked in these figures, corresponding to *pwp* = 0 kPa, indicates the position of the g_{wt} as it changes over time, with a constant suction of 1250 kPa at the top. This shows

that the depth of g_{wt} mainly depends on the soil permeability and external environmental conditions such as temperature, humidity, and moisture, leading to the development of suction. Hence, in this study, the g_{wt} was evaluated from the *pwp*-distribution curves (shown in Figure 6a–d) for cases Ψ-1250 kPa, Ψ-500 kPa, Ψ-5000 kPa, and Ψ-2500 kPa, respectively. These curves present the pwp distribution along the depth of subgrade at different time frames varying from 1–180 days. For instance, consider the case Ψ-5000 kPa as shown in Figure 6c; higher suctions are developed at the top layers in the initial days, and with the increase in a number of days (t), an even distribution of suction occurs. Further, the distribution of *pwp* along the depth in these figures can be described as an incipient parabolic curve transitioning into a linear trend, in which the parabolic part refers to negative pwps (suction) and the linear part refers to positive *pwp*s. The g_{wt} was obtained at the depth where *pwp* = 0 kPa. Figure 7a shows the variation trend of g_{wt} depth with the number of days (t) evaluated from the pwp curves (Figure 6a–d). The evaluated d_{gwt} followed the trend of the power curve represented by Equation (10):

$$d_{gwt} = at^n \tag{10}$$

where a and n are fitting parameters depending on the suction at the top and subgrade soil parameters. Furthermore, the pwp at the base of the subgrade (i.e., at 5 m of depth) decreased with the increase in top suction and the number of days, as shown in Figure 7b. This indicates that, as suction increases, the effective stresses in the subgrade also increase. Consequently, the stiffness and shear strength of the soil increase and subgrades can sustain a higher structural load. However, from our previous studies [39,44], it was observed that at suctions of more than 2000 kPa, the expansive soil could experience volume changes leading to higher shrinkage. In addition, at lower suctions less than 700 kPa, the expansive soil may swell. Considering these factors, the zone of probable shrinkage (ZOPS) and zone of probable swelling (ZOPSW) are identified in Figure 6a–d. In pavement design involving unsaturated subgrades, the zones of probable shrinkage and swelling are critical in determining the long-term performance and durability of the pavement structure. This is particularly relevant in regions with high soil suctions (e.g., 2000 kPa or higher) where significant moisture fluctuations result in volumetric changes in the soil, causing pavement distress. In soils with high suction, significant volume changes are likely when moisture content shifts, increasing the vulnerability of the pavement to both swelling and shrinkage during dry–wet cycles. These zones can help identify the optimal depth for implementing alternative solutions and provide cost-effective approaches. Summarizing the significance of these curves, they play a crucial role in assessing the depth of the groundwater table and the condition of the subgrade soil.

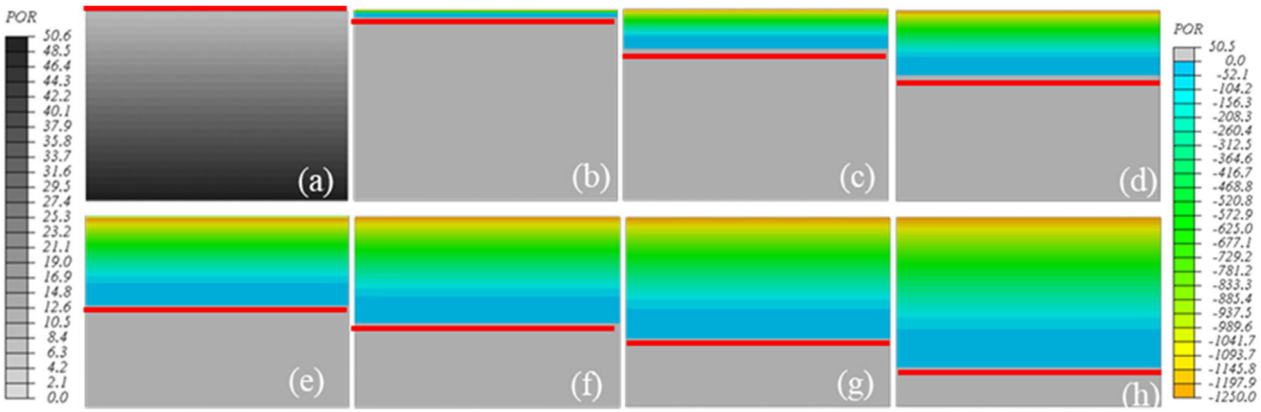

Figure 5. Contours of *pwp* variation during drying along the depth of a subgrade with suction 1250 kPa at top: (**a**) geostatic step, (**b**) 1 day, (**c**) 10 days, (**d**) 30 days, (**e**) 60 days, (**f**) 90 days, (**g**) 120 days, and (**h**) 180 days.

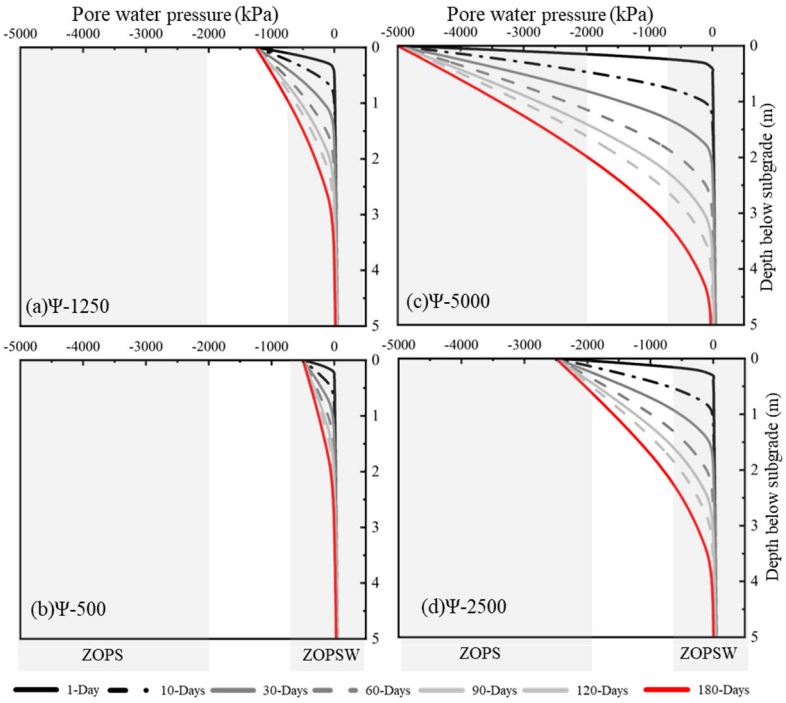

Figure 6. Pore water-pressure-distribution curves for subgrade with suction at top Ψ_t (**a**) Ψ_t = 1250 kPa, (**b**) Ψ_t = 500 kPa, (**c**) Ψ_t = 5000 kPa, and (**d**) Ψ_t = 2500 kPa.

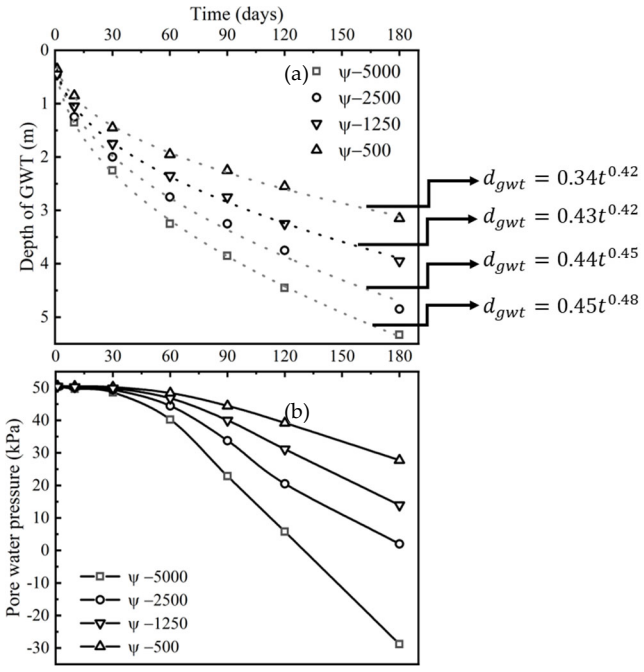

Figure 7. Variations of (**a**) d_{gwt} vs. time (days); (**b**) *pwp* vs. time (days) at a depth of 5 m.

8.1.2. Pavement-Deformation Response During Drying of Subgrade

A flexible pavement's major structural distress types are rutting and fatigue behavior due to cyclic wheel loading. In this context, it was essential to evaluate the rutting and fatigue behavior, which can be assessed from the surface-deflection profile along the width of the AC layer and the horizontal strain profile along the width at the interface of the base and AC layer, respectively. In addition, stresses transferred to the subgrade were also crucial in evaluating the structural performance of the pavements. Figure 6 shows pwp

distribution profiles of the unsaturated subgrade during drying, through which d_{gwt} were estimated. In step 3, cyclic wheel loading of 10,000 cycles was applied on the pavement with unsaturated subgrade after 1, 30, 90, and 180 days, respectively, and the corresponding pavement response was evaluated.

Figure 8a–d indicates the maximum surface deflections under cyclic wheel load were equal to 12 mm, 10.88 mm, 10.05 mm, and 8.38 mm for the cases Ψ-500 kPa, Ψ-1250 kPa, Ψ-2500 kPa, and Ψ-5000 kPa, respectively, after 180 days of drying. It was evident that, as the g_{wt} falls, the maximum surface deflection decreases. Further, the results shown in Figure 7 indicated a decrease in d_{gwt} below the subgrade formation level ranging from 0.34 m to 3.15 m, 0.45 m to 3.95 m, 0.45 m to 4.8 5m, and 0.45 m to 5.45 m for the cases Ψ-500 kPa, Ψ-1250 kPa, Ψ-2500 kPa, and Ψ-5000 kPa, respectively. Accordingly, the maximum surface deflection due to the applied wheel load after 180 days of drying decreases by 43%, 45.48%, 43%, and 56%, respectively, in comparison to respective 1-day drying. It should be noted that with the increase in suction, elapsed time, and d_{gwt}, the subgrade will be in an unsaturated condition such that the stiffness of the subgrade increases with the increase in suction [21]. Furthermore, when the USDFLD subroutine is not applied in the conventional Mohr–Coulomb behavior of the subgrade, the peak deflection and horizontal strain are observed to reach 9.2 mm and 0.0015, respectively. In the short term, matric suction plays a more significant role during drying, as rapid moisture changes cause the soil to deform more than conventional methods predict. As moisture stabilizes over time, both methods produce similar long-term predictions since suction effects reduce and the soil's behavior becomes more predictable. For instance, after 180 days of drying, the surface deflections at suctions of 5000 kPa and 2500 kPa are 8.38 mm and 10.05 mm, respectively, which are comparable to the 9.2 mm deflection from the conventional approach. However, the results from the conventional approach tend to be underestimated because the material behavior is assumed to be elastic-perfectly plastic, without considering changes in the elastic modulus or cohesion due to suction. This highlights the crucial role of evaluating *pwp* distribution and d_{gwt} in assessing the long-term performance of pavements.

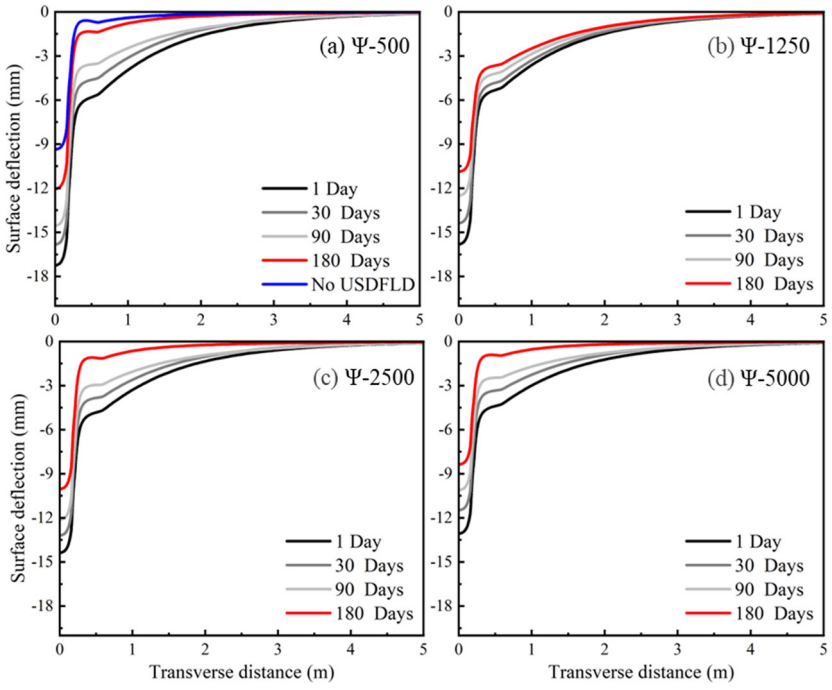

Figure 8. Surface-deflection profile of pavement at peak load time during subgrade drying (**a**) Ψ_t = 500 kPa, (**b**) Ψ_t = 1250 kPa, (**c**) Ψ_t = 2500 kPa, and (**d**) Ψ_t = 5000 kPa.

Figure 9a–d indicates that with an increase in the d_{gwt} below the subgrade formation level, the horizontal strains developed below the AC layer decreased. Further, the vertical stress developed due to the applied wheel load is obtained at the top of the subgrade, as represented by a red dot (S22) in Figure 2. Higher vertical stresses were observed for the unsaturated subgrade with a d_{gwt} at the top in the initial days. In addition, with the fall in the d_{gwt}, the vertical stresses at the top of the unsaturated subgrade due to wheel load at peak time decreased, as shown in Figure 10. The subgrade soil sustains higher external loads because, with the fall in d_{gwt}, more suction develops in the unsaturated subgrade, resulting in increased stiffness and strength of the soil.

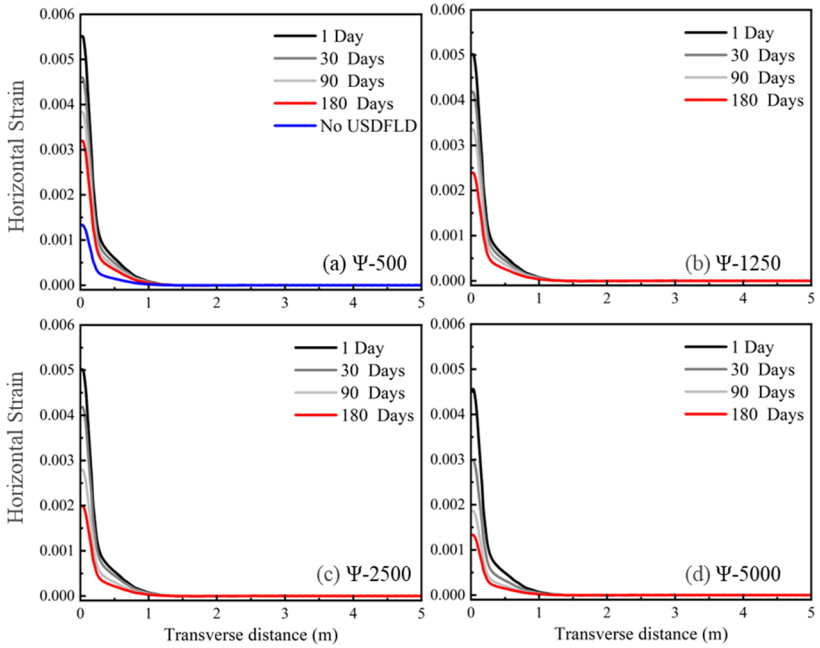

Figure 9. Horizontal strain profile below the AC layer at peak load time during subgrade drying (**a**) Ψ_t = 500 kPa, (**b**) Ψ_t = 1250 kPa, (**c**) Ψ_t = 2500 kPa, and (**d**) Ψ_t = 5000 kPa.

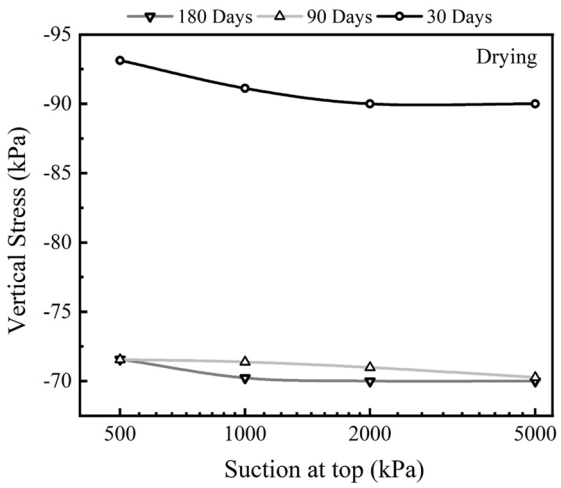

Figure 10. Vertical stresses at the top of the unsaturated subgrade at peak load time during subgrade drying.

8.2. The Effect of Subgrade Wetting

In this analysis, along with steps 1 and 2 outlined in Section 8.1, the following steps were conducted: (3) wetting of the subgrade with a *pwp* of 0 at the surface, and (4) application of 10,000 cycles of wheel loading at the surface. It is important to note that in step 3,

the g_{wt} is not at the top. Rather, the subgrade begins to saturate with an initial g_{wt} at a specific depth, depending on the conditions of step 2.

8.2.1. Changes in g_{wt} with Subgrade Suction During Wetting

During the drying process, the g_{wt} decreases, and suction (negative *pwp*) in the unsaturated soil changes along the depth of the subgrade. Further, two different time durations (90 and 180 days) during the drying process in step 2 have been chosen to evaluate the initial g_{wt}. Subsequently, in step 3, the subgrade was allowed to saturate, and the corresponding analysis cases Ψ2500-D180, Ψ2500-D90, Ψ5000-D180, and Ψ5000-D90 are presented. For instance, Ψ5000-D180 represents the results of 180 days of drying at 5000 kPa suction at the top and subsequent wetting. The contour of negative pwp (suction) distribution for the case Ψ5000-D180 after the completion of step 2 is shown in Figure 11a. The contour depicts the distribution of negative *pwp*, ranging from −5000 kPa at the top surface to −28 kPa at a depth of 5 m. Since the g_{wt} is located beyond 5 m of depth, the precise value of the d_{gwt} is estimated as 5.45 m using Equation (10). In the succeeding Figure 11b–h, the *pwp* contour portrays the case Ψ5000-D180, where the subgrade is allowed to saturate for 180 days. Figure 11b–d, representing the scenarios at 1, 10, and 30 days, respectively, illustrate the saturation of top layers and higher suctions beyond that. Over time, as saturation persists, moisture penetrates deeper layers, leading to a rise in g_{wt}, as shown in Figure 11e–h. Nevertheless, it is crucial to acknowledge that the higher initial suction (5000 kPa) in this scenario results in a subgrade-saturation process that exceeds the 180-day analysis duration. This type of behavior depends on the initial suction at the top layers of the subgrade before the start of saturation and the duration of the saturation process. Summarizing this behavior, Figure 12a–d presents the *pwp*-distribution curves during subgrade wetting at different time periods for the cases of Ψ2500-D180, Ψ2500-D90, Ψ5000-D180, and Ψ5000-D90. Figure 12a shows the *pwp* distribution along the depth of the ubgrade with an initial suction of 2500 kPa for 180 days before saturation. The *pwp* distribution in the initial time durations of wetting depicts an incipient c-type curve transitioning into a linear trend and, at later durations, showing a linear trend indicating the saturation level of the subgrade. Similarly, in the Ψ2500-D90, as the drying duration is lesser, the subsequent wetting leads to a faster saturation, as shown in Figure 12b. Moreover, Figure 12c,d exhibits similar behavior with higher initial suction of 5000 kPa for 180 and 90 days, respectively. In these cases, the subgrade saturation in the top layers indicates the dependency of d_{gwt} and subgrade saturation on the initial suction. Furthermore, these curves can be used to identify the zones of probable top-layer subgrade swelling (ZOPTSW). One of our previous studies [39] indicated that subgrade materials with higher initial suction before saturation lead to the development of higher swelling characteristics during the wetting process. This study indicated that swelling potential and swelling pressure varied from 5–15% and 50–100 kPa for variation of initial suction from 1000–5000 kPa. In Figure 12a–d, the dotted horizontal line represents the depth of the subgrade prone to increased swelling, particularly during the initial durations of 1–60 days, depending on the initial suction. The respective values for Ψ2500-D180, Ψ2500-D90, Ψ5000-D180, and Ψ5000-D90 are 1.8 m, 1.2 m, 3 m, and 2.1 m. Notably, the case Ψ5000-D180 exhibits a more extensive depth of potential swelling, attributed to higher initial suction and lower permeability, resulting in increased saturation in the top layers.

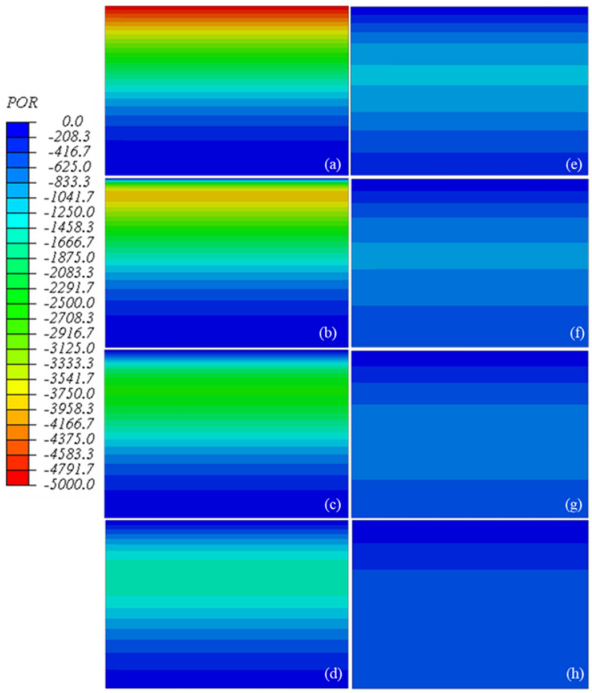

Figure 11. Contours of *pwp* variation during wetting along the depth of a subgrade with initial suction Ψ_i = 5000 kPa at the top: (**a**) step 2, (**b**) 1 day, (**c**) 10 days, (**d**) 30 days, (**e**) 60 days, (**f**) 90 days, (**g**) 120 days, and (**h**) 180 days.

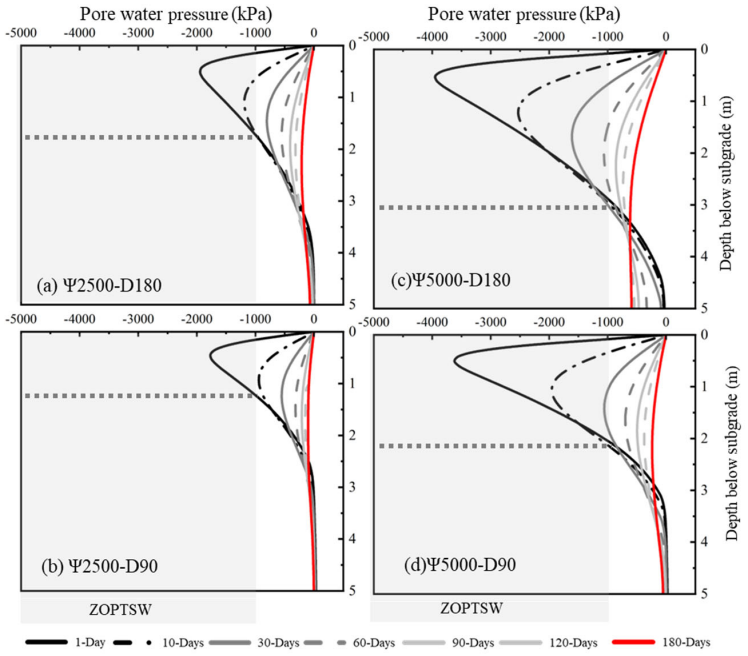

Figure 12. Pore water-pressure-distribution curves for subgrade during wetting with initial suction at the top Ψ_i : (**a**) After Step 2, initial suction, Ψ_i = 2500 kPa, and wetting in step 3 for 180 days; (**b**) after step 2, initial suction, Ψ_i = 2500 kPa, and wetting in step 3 for 90 days; (**c**) after step 2, initial suction, Ψ_i = 5000 kPa, and wetting in step 3 for 18 days; (**d**) after step 2, initial suction, Ψ_i = 5000 kPa, and wetting in step 3 for 90 days.

8.2.2. Pavement-Deformation Response During Wetting of Subgrade

After drying the subgrade with enforced suction in step 2, the subgrade was allowed to fully saturate the subgrade formation level in step 3, with elapsed time varying from

1–180 days. Later, cyclic wheel loading for 10,000 cycles was applied at the top in step 4 with saturated subgrade after 1, 30, 90, and 180 days, respectively, and the corresponding pavement response was evaluated. The corresponding surface-deflection profiles for different time durations of the pavement are provided in Figure 13a–d. For instance, the findings presented in Figure 13a demonstrate that, with the wetting of an unsaturated subgrade starting from an initial suction of 500 kPa, the surface deflection resulting from the applied wheel load was 19.9 mm for the saturated subgrade over a 180-day period. Further, in the case of the conventional mechanistic approach without employing USDFLD, the observed peak deflection and horizontal strain are 18.2 mm and 0.0055, respectively. These values overestimate the results for the first 1–90 days and underestimate the critical 180-day saturation duration, as illustrated in Figures 13a and 14a. Furthermore, the results illustrated in Figure 13a–d indicate that with an increase in subgrade saturation time, they range from 1 to 180 days for the cases of initial suction Ψ_i-500 kPa, Ψ_i-1250 kPa, Ψ_i-2500 kPa, and Ψ_i-5000 kPa, respectively. Figure 13e shows the percentage change in surface deflection due to applied wheel loads compared to the respective initial cases after 180 days of drying, with suction levels of 500, 1250, 2500, and 5000 kPa, and deflection caused by wheel loads after saturation periods ranging from 1 to 180 days. As depicted in Figure 13e, higher initial suctions (5000 kPa) lead to a more pronounced increase in surface deflection following wetting. The subgrade shows a 98% rise in peak-surface deflections at 180 days under wheel loads compared to the initial case, indicating a substantial weakening as the subgrade nears saturation. On the other hand, with lower initial suctions (1250 kPa), the increase in surface deflection after wetting is smaller, as the subgrade's moisture content does not change drastically. The surface deflection due to applied wheel loads rises by approximately 78% at 180 days of wetting, which is notably lower than the 5000 kPa scenario. It should be noted that the % increase for the cases of higher initial suctions in step 2 is higher in comparison to other cases. Further, the saturation process is controlled by the infiltration capacity of the subgrade soil during wetting. It is the measure of the maximum rate of water at which water enters into the soil during wetting. The infiltration capacity mainly depends on unsaturated permeability and suction. However, at higher suction, the infiltration capacity is greater for the soil, irrespective of the permeability [45].

Moreover, the present study does not take side drainage into account, limiting the drainage capacity of subgrade layers. Hence, at higher suctions, the top layers of the subgrade will be saturated quickly such that the stiffness of the top layers decreases predominantly. Due to this phenomenon, a higher increase in vertical deflections is observed. Similarly, horizontal strains are increased with elapsed saturation time and rise in d_{gwt} as shown in Figure 14a–d. Swelling and shrinking of the subgrade might occur with an increase in suction and subsequent saturation of the top layers of the subgrade. These subsequent suction and saturation increased horizontal strains at the bottom of the AC layer. This behavior can be attributed to the top-layer stiffness reduction. Further, it was observed that vertical stresses at the top of the subgrade are predominantly high due to applied wheel loading, as provided in Figure 15. The vertical stress increased with the increase in elapsed saturation duration and rise in d_{gwt}. The maximum vertical stress was 86.76 kPa for the saturated subgrade, having an initial suction of 500 kPa and d_{gwt} of 3.15 m. In the case of an initial suction of 5000 kPa, the subgrade is in the early stages of saturation after 30 days of wetting, as shown in Figure 11d. Initially, the moisture did not penetrate deeply, leading to softening and stiffness loss in the upper layers. However, by 90 and 180 days, moisture has infiltrated deeper into the subgrade. The deeper layers, with residual suction, continue to exhibit higher stiffness, while the upper layers consolidate due to the increased moisture. This leads to greater vertical stress due to applied wheel loads compared to the 30-day period. Further, in the case of an initial suction of 2500 kPa, the subgrade reaches saturation more quickly, causing a rapid drop in suction and a corresponding loss of stiffness. This faster saturation softens the soil, leading to increased vertical stress concentrations as the subgrade struggles to distribute the load effectively. The rapid reduction in suction and stiffness under the load can result in higher localized

stresses. Summarizing the observations, the factors governing the subgrade behavior are external environmental conditions that lead to the development of suction, drying/wetting duration, and d_{gwt}.

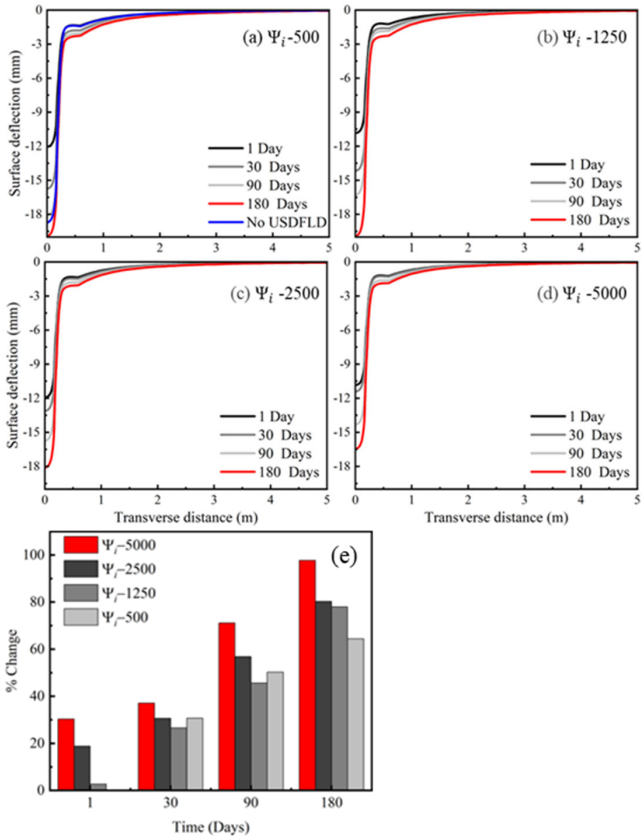

Figure 13. Surface-deflection profile of pavement at peak load time during subgrade wetting (**a**) Ψ_i = 500 kPa, (**b**) Ψ_i = 1250 kPa, (**c**) Ψ_i = 2500 kPa, (**d**) Ψ_i = 5000 kPa, and (**e**) % change with days.

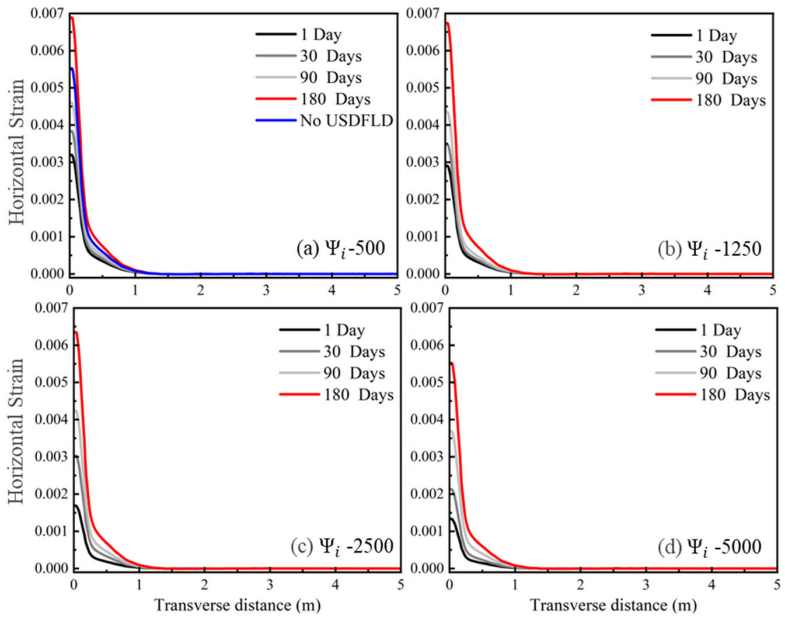

Figure 14. Horizontal-strain profile below the AC layer at peak load time during subgrade wetting: (**a**) Ψ_i = 500 kPa, (**b**) Ψ_i = 1250 kPa, (**c**) Ψ_i = 2500 kPa, and (**d**) Ψ_i = 5000 kPa.

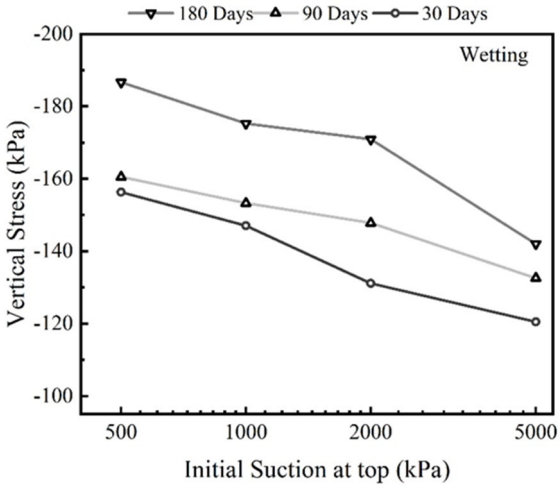

Figure 15. Vertical stresses at the top of the subgrade during wetting.

9. Conclusions

The present study focused on the performance of flexible pavements with unsaturated and saturated subgrade. Keeping this in view, the numerical analysis was conducted on the pavement model to evaluate the factors affecting the subgrade and structural performance of the flexible pavement. The influence of subgrade suction variations on changes in d_{gwt} during drying and wetting, and their subsequent impact on the structural performance of pavements, is explored through the FE simulations. The following conclusions based on parametric evaluation and sensitivity analysis can be drawn from the present study:

1. Coupled pore-pressure deformation analysis is required to properly evaluate the impact of the suction on the structural response of flexible pavements with unsaturated and saturated subgrades under heavy vehicular wheel loads during the drying and wetting phases.
2. The d_{gwt} is determined by suction and elapsed duration during drying. However, in the wetting phase, the top layers of the subgrade saturate, and as the duration increases, the d_{gwt} gradually rises in accordance with the evolution of the *pwp*-distribution profile.
3. An increase in stiffness occurs in the subgrade due to the development of suction during drying. As a result, the structural performance of the pavement increased. In addition, d_{gwt} also plays an important role apart from the suction in evaluating the structural performance of the pavement. This indicates the importance of maintaining groundwater clearance for pavements.
4. The analysis demonstrates an increase in maximum vertical deflection to 98% when the subgrade is fully saturated from an initial d_{gwt} of 5.45 m with an initial suction of 5000 kPa.
5. Increased vertical stresses on the top of the subgrade have been observed due to the application of wheel loading in the wetting phase.

Recommendations and Future scope of work

- Incorporation of Suction Effects: Flexible pavement designs in semi-arid and arid regions should incorporate suction variations and groundwater table fluctuations to enhance long-term performance.
- Maintenance of Groundwater Table Depth: Regular monitoring and maintenance of groundwater table depth with appropriate side drainage systems are crucial for minimizing pavement deformation and ensuring durability.
- 3D Numerical Simulations and Cost-effective Analysis: Exploration of 3D simulations to better capture the complexity of pavement behavior, reducing computation time while increasing accuracy and integrating a cost analysis to assess the effectiveness of

alternative designs and maintenance approaches. This will complement the technical findings from numerical simulations and provide a more robust decision-making framework for pavement design in regions with highly variable moisture conditions.
- Long-term Monitoring: Implementation of long-term field-monitoring systems for pavement deformation, and groundwater variations would provide valuable data for validating numerical models.
- Application to Other Climate Zones: Extending the study to other climatic conditions, such as tropical or polar regions, will help in understanding pavement behavior under different moisture regimes.
- Sustainable Pavement Materials: Analysis of sustainable pavement materials in combination with geosynthetics that perform well under varying suction conditions, contributing to both performance and environmental sustainability.

Author Contributions: Conceptualization, S.R.K. and A.M.; methodology, S.R.K., A.M. and S.L.; software, S.R.K.; validation, S.R.K.; formal analysis, S.R.K.; investigation, S.R.K.; resources, A.M. and S.L.; data curation, S.R.K.; writing—original draft preparation, S.R.K.; writing—review and editing, A.M. and S.L.; visualization, S.R.K.; supervision, A.M. and S.L.; project administration, A.M. and S.L.; funding acquisition, S.L. All authors have read and agreed to the published version of the manuscript.

Funding: This research received funding from The Slovenian Research Agency (ARRS) Programme group P2-0273, Core funding Z1-1858, and the Development Funding Pillar (RSF).

Institutional Review Board Statement: Not applicable.

Informed Consent Statement: Not applicable.

Data Availability Statement: All data, models, or code generated or used during the study are available from the corresponding author by request.

Acknowledgments: The first author is grateful to the Visvesvaraya National Institute of Technology, Nagpur, for providing the necessary support to conduct this research work. Additionally, the authors express gratitude for the support provided by the Ministry of Higher Education, Science, and Technology of the Republic of Slovenia, as well as The Slovenian Research Agency (ARRS) Programme group P2-0273, Core funding Z1-1858, and Development funding pillar (RSF), which financially supported the project PE-Harmony.

Conflicts of Interest: The authors declare no conflicts of interest.

Appendix A

```
**              USDFLD              **
* User subroutine
      SUBROUTINE USDFLD (FIELD, STATEV, PNEWDT, DIRECT, T, CELENT,
     1 TIME, DTIME, CMNAME, ORNAME, NFIELD, NSTATV, NOEL, NPT, LAYER,
     2 KSPT, KSTEP, KINC, NDI, NSHR, COORD, JMAC, JMATYP, MATLAYO,
     3 LACCFLA)
C
      INCLUDE 'ABA_PARAM.INC'
C
      CHARACTER*80 CMNAME, ORNAME
      CHARACTER*3 FLGRAY(15)
      DIMENSION FIELD (NFIELD), STATEV (NSTATV), DIRECT (3,3),
     1 T (3,3), TIME (2)
      DIMENSION ARRAY (15), JARRAY (15), JMAC (*), JMATYP (*),
     1 COORD (*)
C
C Get pore water pressure from last completed increment:
      CALL GETVRM ('POR', ARRAY, JARRAY, FLGRAY, JRCD, JMAC, JMATYP,
     1 MATLAYO, LACCFLA)
```

```
      POR1 = ARRAY (1)
C
C Store the accumulated pore water pressure as field variable:
      FIELD (1) = POR1
C
      RETURN
      END
```

References

1. Knott, J.F.; Jacobs, J.M.; Sias, J.E.; Kirshen, P.; Dave, E.V. A Framework for Introducing Climate-Change Adaptation in Pavement Management. *Sustainability* **2019**, *11*, 4382. [CrossRef]
2. Kumar, R.; Kuttippurath, J.; Gopikrishnan, G.S.; Kumar, P.; Varikoden, H. Enhanced Surface Temperature over India during 1980–2020 and Future Projections: Causal Links of the Drivers and Trends. *NPJ Clim. Atmos. Sci.* **2023**, *6*, 164. [CrossRef]
3. Kumar, M.; Hayano, K. Variation of the Groundwater Table within Indian Railway Embankments in Consideration of Climate Change. *Sustainability* **2024**, *16*, 6143. [CrossRef]
4. *Observed Climate Variability and Change over the Indian Region*; Rajeevan, M.N., Nayak, S., Eds.; Springer: Singapore, 2017; ISBN 978-981-10-2530-3.
5. Swarna, S.T.; Hossain, K. Climate Change Impact and Adaptation for Highway Asphalt Pavements: A Literature Review. *Can. J. Civ. Eng.* **2022**, *49*, 1109–1120. [CrossRef]
6. Wang, W.; Wang, L.; Miao, Y.; Cheng, C.; Chen, S. A Survey on the Influence of Intense Rainfall Induced by Climate Warming on Operation Safety and Service Life of Urban Asphalt Pavement. *J. Infrastruct. Preserv. Resil.* **2020**, *1*, 4. [CrossRef]
7. Rashadul Islam, M.; Vallejo, M.J.; Tarefder, R.A. Crack Propagation in Hot Mix Asphalt Overlay Using Extended Finite-Element Model. *J. Mater. Civ. Eng.* **2017**, *29*, 04016296. [CrossRef]
8. Wang, H.; Wang, J. Numerical Analysis of Surface Crack Propagation in Flexible Pavements Using XFEM and Cohesive Zone Model. *Int. J. Pavement Res. Technol.* **2014**, *7*, 178–184.
9. Luo, R.; Prozzi, J.A. Development of Longitudinal Cracks on Pavement over Shrinking Expansive Subgrade. *Road Mater. Pavement Des.* **2010**, *11*, 807–832. [CrossRef]
10. Saad, B. Analysis of Excess Water Impact on the Structural Performance of Flexible Pavements. *Int. J. Pavement Eng.* **2014**, *15*, 409–426. [CrossRef]
11. Chen, L.; Bulut, R. Numerical Analysis of Horizontal Moisture Barriers in Pavements Constructed on Expansive Soils. *Procedia Eng.* **2016**, *143*, 229–236. [CrossRef]
12. Chen, L.; Bulut, R. Numerical Analysis of the Effects of Cracks on the Moisture-Diffusion Coefficient of Unsaturated Soils. *Int. J. Geomech.* **2017**, *17*, 1–6. [CrossRef]
13. Sun, D.M.; Li, X.M.; Feng, P.; Zang, Y.G. Stability Analysis of Unsaturated Soil Slope during Rainfall Infiltration Using Coupled Liquid-Gas-Solid Three-Phase Model. *Water Sci. Eng.* **2016**, *9*, 183–194. [CrossRef]
14. Batali, L.; Andreea, C. Slope Stability Analysis Using the Unsaturated Stress Analysis. Case Study. *Procedia Eng.* **2016**, *143*, 284–291. [CrossRef]
15. Fatahi, B.; Khabbaz, H.; Indraratna, B. Modelling of Unsaturated Ground Behaviour Influenced by Vegetation Transpiration. *Geomech. Geoengin.* **2014**, *9*, 187–207. [CrossRef]
16. Tang, A.M.; Hughes, P.N.; Dijkstra, T.A.; Askarinejad, A.; Brenčič, M.; Cui, Y.J.; Diez, J.J.; Firgi, T.; Gajewska, B.; Gentile, F.; et al. Atmosphere-Vegetation-Soil Interactions in a Climate Change Context; Impact of Changing Conditions on Engineered Transport Infrastructure Slopes in Europe. *Q. J. Eng. Geol. Hydrogeol.* **2018**, *51*, 156–168. [CrossRef]
17. Oh, W.T.; Vanapalli, S.K.; Puppala, A.J. Semi-Empirical Model for the Prediction of Modulus of Elasticity for Unsaturated Soils. *Can. Geotech. J.* **2009**, *46*, 903–914. [CrossRef]
18. Cheng, X.; Tan, M.; Vanapalli, S. Simple Approaches for the Design of Shallow and Deep Foundations for Unsaturated Soils II: Numerical Techniques. *Indian Geotech. J.* **2021**, *51*, 115–126. [CrossRef]
19. Vanapalli, S.K.; Mohamed, F.M.O. Bearing Capacity of Model Footings in Unsaturated Soils. In *Experimental Unsaturated Soil Mechanics*; Springer: Berlin/Heidelberg, Germany, 2007; pp. 483–493.
20. Sawangsuriya, A.; Edil, T.B.; Bosscher, P.J. Modulus−suction−moisture Relationship for Compacted Soils. *Can. Geotech. J.* **2008**, *45*, 973–983. [CrossRef]
21. Mendoza, C.E.; Colmenares, J.E. Influence of the Suction on the Stiffness at Very Small Strains. In *Proceedings of the Unsaturated Soils 2006*; American Society of Civil Engineers: Reston, VA, USA, 2006; pp. 529–540.
22. Cheng, X.; Vanapalli, S.K. A Numerical Technique for Modeling the Behavior of Single Piles in Unsaturated Soils. *MATEC Web Conf.* **2021**, *337*, 03012. [CrossRef]
23. Oh, W.T.; Vanapalli, S.K. Modelling the Applied Vertical Stress and Settlement Relationship of Shallow Foundations in Saturated and Unsaturated Sands. *Can. Geotech. J.* **2011**, *48*, 425–438. [CrossRef]
24. Sheng, D.; Gens, A.; Fredlund, D.G.; Sloan, S.W. Unsaturated Soils: From Constitutive Modelling to Numerical Algorithms. *Comput. Geotech.* **2008**, *35*, 810–824. [CrossRef]

25. Fredlund, D.; Gitirana, G., Jr. Unsaturated Soil Mechanics as a Series of Partial Differential Equations. *Proc. Int. Conf. Probl. Soils* **2005**, *25*, 27.
26. Gallipoli, D.; Gens, A.; Chen, G.; D'Onza, F. Modelling Unsaturated Soil Behaviour during Normal Consolidation and at Critical State. *Comput. Geotech.* **2008**, *35*, 825–834. [CrossRef]
27. Nuth, M.; Laloui, L. Advances in Modelling Hysteretic Water Retention Curve in Deformable Soils. *Comput. Geotech.* **2008**, *35*, 835–844. [CrossRef]
28. Fredlund, D.G.; Rahardjo, H. *Soil Mechanics for Unsaturated Soils*; John Wiley & Sons, Inc.: Hoboken, NJ, USA, 1993; ISBN 9780470172759.
29. Prozzi, J.A.; Luo, R. Using Geogrids to Minimize Reflective Longitudinal Cracking on Pavements over Shrinking Subgrades. *Transp. Res. Rec. J. Transp. Res. Board* **2007**, *2004*, 99–110. [CrossRef]
30. Wang, Y.; Gu, Y.; Liu, J. A Domain-Decomposition Generalized Finite Difference Method for Stress Analysis in Three-Dimensional Composite Materials. *Appl. Math. Lett.* **2020**, *104*, 106226. [CrossRef]
31. Garcia, F.E.; Bray, J.D. Distinct Element Simulations of Earthquake Fault Rupture through Materials of Varying Density. *Soils Found.* **2018**, *58*, 986–1000. [CrossRef]
32. Hamdhan, I.N.; Schweiger, H.F. Finite Element Method–Based Analysis of an Unsaturated Soil Slope Subjected to Rainfall Infiltration. *Int. J. Geomech.* **2012**, *13*, 653–658. [CrossRef]
33. Li, K.; Nowamooz, H.; Chazallon, C.; Migault, B. Finite Element Modelling of the Mechanical Behaviour of Unsaturated Expansive Soils Subjected to Wetting and Drying Cycles with Shakedown Concept. *Eur. J. Environ. Civ. Eng.* **2017**, *24*, 17–33. [CrossRef]
34. Kabir, H.; Aghdam, M.M. A Robust Bézier Based Solution for Nonlinear Vibration and Post-Buckling of Random Checkerboard Graphene Nano-Platelets Reinforced Composite Beams. *Compos. Struct.* **2019**, *212*, 184–198. [CrossRef]
35. Fredlund, D.G.; Rahardjo, H.; Fredlund, M.D. *Unsaturated Soil Mechanics in Engineering Practice*; John Wiley & Sons, Inc.: Hoboken, NJ, USA, 2012; ISBN 9781118280492.
36. White, T.D.; Haddock, J.E.; Hand, A.J.T.; Fang, H. NCHRP REPORT 468: Contributions of Pavement Structural Layers to Rutting of Hot Mix Asphalt Pavements. 2002. Available online: https://onlinepubs.trb.org/onlinepubs/nchrp/nchrp_rpt_468-a.pdf (accessed on 19 September 2024).
37. Gu, F.; Luo, X.; Luo, R.; Lytton, R.L.; Hajj, E.Y.; Siddharthan, R.V. Numerical Modeling of Geogrid-Reinforced Flexible Pavement and Corresponding Validation Using Large-Scale Tank Test. *Constr. Build. Mater.* **2016**, *122*, 214–230. [CrossRef]
38. Oh, W.T.; Vanapalli, S.K. A Simple Method to Estimate the Bearing Capacity of Unsaturated Fine-Grained Soils. In *Proceedings of the GeoHalifax2009*; 2009; pp. 234–241. Available online: https://members.cgs.ca/documents/conference2009/GeoHalifax09/pdfs/32.pdf (accessed on 19 September 2024).
39. Karumanchi, S.R.; Singh, D.K.; Mandal, A. Study on Swelling and Shrinkage Behaviour of Unsaturated Soils from Material Characteristics. *Road Mater. Pavement Des.* **2020**, *21*, 1274–1292. [CrossRef]
40. Leonardi, R.P.; Calvarano, L.S. Numerical Analysis of Flexible Pavement Reinforced with Geogrids. In *Proceedings of the Airfield and Highway Pavements*; American Society of Civil Engineers: Reston, VA, USA, 2006; pp. 115–126.
41. Vanapalli, S.; Oh, W. A Model for Predicting the Modulus of Elasticity of Unsaturated Soils Using the Soil-Water Characteristic Curve. *Int. J. Geotech. Eng.* **2010**, *4*, 425–433. [CrossRef]
42. Oh, W.T.; Vanapalli, S.K. Modeling the Stress versus Settlement Behavior of Shallow Foundations in Unsaturated Cohesive Soils Extending the Modified Total Stress Approach. *Soils Found.* **2018**, *58*, 382–397. [CrossRef]
43. Li, J.; Zheng, J.; Yao, Y.; Zhang, J.; Peng, J. Numerical Method of Flexible Pavement Considering Moisture and Stress Sensitivity of Subgrade Soils. *Adv. Civ. Eng.* **2019**, *2019*. [CrossRef]
44. Karumanchi, S.R.; Mandal, A. Moisture Variations and Its Effect on Shrinkage and Swelling Characteristics of Unsaturated Soil. *Eur. J. Environ. Civ. Eng.* **2020**, *24*, 1785–1801. [CrossRef]
45. Gavin, K.; Xue, J. A Simple Method to Analyze Infiltration into Unsaturated Soil Slopes. *Comput. Geotech.* **2008**, *35*, 223–230. [CrossRef]